coatings

MDPI

Article

Rebound Dynamics of Two Droplets Successively Impacting an Inclined Surface

Dian-Ji Lin [1,2], Ling-Zhe Zhang [1,2], Meng-Chao Yi [1,2], Xin Wang [1,2], Shu-Rong Gao [1,2], Yan-Ru Yang [1,2] and Xiao-Dong Wang [1,2,*]

1 Research Center of Engineering Thermophysics, North China Electric Power University, Beijing 102206, China; victorlin@ncepu.edu.cn (D.-J.L.); zhanglingzhe@ncepu.edu.cn (L.-Z.Z.); yimengchao@ncepu.edu.cn (M.-C.Y.); 1152102021@ncepu.edu.cn (X.W.); 53002421@ncepu.edu.cn (S.-R.G.); cathyyang888@gmail.com (Y.-R.Y.)

2 State Key Laboratory of Alternate Electrical Power System with Renewable Energy Sources, North China Electric Power University, Beijing 102206, China

* Correspondence: wangxd99@gmail.com; Tel.: +86-010-6232-1277

Received: 19 May 2020; Accepted: 22 June 2020; Published: 24 June 2020

Abstract: The dynamic behaviors of two droplets successively impacting inclined surfaces are simulated by a three-dimensional pseudopotential lattice Boltzmann model based on multi-relaxation-time. The effect of velocity ratio of two successive droplets on the contact time is investigated and two rebounding regimes are identified depending on whether the coalesced droplet retouches the surface or not. Increasing the velocity ratio leads to a stronger interaction between the two droplets and the phenomenon of coalesced droplet retouching the surface is observed when the velocity ratio exceeds a threshold, resulting in a longer contact time. An outcome map of droplet rebounding is obtained at various velocity ratios and contact angles of surface. It is found that the coalesced droplet cannot rebound from the surface at a larger velocity ratio and a lower contact angle of surface. Furthermore, the effect of the length between impact points on the contact time is exhibited, and a longer length is beneficial to coalesced droplet rebounding.

Keywords: rebound dynamics; two droplets; inclined surface; impact; superhydrophobic surface

1. Introduction

The phenomenon of droplets impacting a solid surface is extensively encountered in various applications like self-cleaning, anti-icing, ink-printing, and spray cooling [1–5]. The impact results, such as the outcomes, contact time, and spreading diameter, are important for the quality of anti-icing, ink-printing, and heat transfer. The impact characteristics of a single droplet are studied intensively and affected by the physical properties of droplet (diameter, viscosity, surface tension), impact velocity, surface properties (wettability, roughness, angle of inclination) [6–9]. In fact, the impact of multi-droplet is more ubiquitous. The impact dynamic behavior of multi-droplet is more complicated, which includes not only impact process, and coalescence process as well. The interaction between the droplets influences the impact results directly, and the investigation on the multi-droplet is increased.

The investigation on impact and coalescence process of multi-droplet starts with the interaction of two droplets. When two successive droplets impact hydrophilic or neutral surface, the velocity field while coalescence, deposition length, and equilibrium shape have attracted much attention. Experiment and lattice Boltzmann simulation were both undertook by Castrejón-Pita et al. [10] to study the interaction between a falling droplet and a sessile one, and the inner velocity field was used to explain the dynamic behavior. The deposition length increased with the center-to-center distance along the horizontal direction. Fujimoto et al. [11] observed a liquid crown after releasing

a droplet above a hemispherical one. The height of liquid crown became larger with increasing the impact velocity. In their later work [12], two falling droplets were utilized with similar velocity, while the vertical spacing between two droplets was different. For a larger vertical spacing, a strong velocity difference between two droplets appeared at the encounter moment, leading to a liquid crown, which was not apparent at the small vertical spacing. Raman et al. [13] applied lattice Boltzmann method to simulate two falling droplets impacting neutral surface. According to the velocity direction before the coalescing moment at different velocity ratios, two interaction models have been defined as in-phase and out-of-phase. The evolution of spreading diameter was influenced by interaction model. Increasing the horizontal spacing and velocity ratio of two droplets enlarged the spreading diameter, while increasing the hydrophobicity had the adverse effect. In ink-printing process, the center-to-center distance along horizontal direction of successive droplets determined the printing quality. The scalloped or even individual droplets are generated at a larger spacing, whereas bulging or stacked coins are formed at a small spacing [14]. To guarantee the uniform and stability of printing line, Stringer and Derby [15] carried out a study combined with experimental and theoretical methods to determine the upper and lower bound of droplet spacing. Zhang et al. [16] obtained the optimal droplet spacing along horizontal direction within the out-of-phase model. If the vertical droplet spacing was enlarged, leading to the interaction model turning to in-phase, the optimal droplet spacing was invalid. For the situation where the direction of impact velocity is not normal to the surface, Raman et al. [17] exhibited that two droplets impacted neutral surface simultaneously and one droplet had a tangential impact velocity component. The effect of impact angle on the deposition length was interpreted. Ahmad et al. [18] illustrated the dynamic behaviors of two successive droplets impacting an inclined surface with contact angle 90°. The effects of droplet spacing along the tangential and lateral direction, and the angle of inclination of surface were discussed. Lattice Boltzmann method were used in the Refs. [16–18].

The investigation on the two successive droplets impacting hydrophobic or superhydrophobic surface is reported insufficiently. Graham et al. [19] performed the coalescence between a falling droplet and a sessile droplet on a solid surface by experiments and simulations. Through increasing the surface hydrophobicity, the sessile droplet merged with the falling one and rebounded from the surface together. While increasing the center-to-center distance along the horizontal direction suppressed the two droplets to rebound, and the mechanism was analyzed by velocity field. Based on the prediction of the maximal spreading diameter of single droplet impacting the superhydrophobic surface, Damak and Varanasi [20] proposed a theoretical model to predict the maximal spreading diameter for drop-on-drop impacting nonwetting surface, which agreed well with experimental results. Yuan et al. [21] found that when a droplet impacted another stationary droplet on a superhydrophobic surface, the coalescent droplet would rotate after rebounding from the surface. The impact velocity and the distance in the vertical direction influenced the formation and the maintain time of the liquid bridge, which determined whether the droplet could rotate after merging. The numerical simulation of two droplets successive impacting a superhydrophobic tube was conducted by Chen et al. [22] via the coupled level set and volume of fluid method. With the impact velocity increased, the outcomes transformed from rebounding to break-up and splash gradually. For droplet impacting the superhydrophobic surface, the contact time is taken as a typical parameter which represents the hydrophobicity of surface. If a single droplet impacts the horizontal smooth superhydrophobic surface, the contact time is not influenced by Weber number ($We = \rho D_0 {v_0}^2/\sigma$) in a range of velocity, where ρ is density, D_0 is diameter, v_0 is the initial velocity, σ is surface tension. Experiments and numerical simulations were conducted by Farhangi et al. [23], which pointed out that when the falling droplet merged with the sessile droplet on the superhydrophobic surface, the rebounding time was independent of the velocity of the falling droplet.

In nature and industrial fields, the droplet encounters various solid surface, such as curve, textured, and inclined surface [24–34]. Compared with the flat horizontal surface, the outcomes are more complex, and the results may be different. Mitra et al. [24] investigated that the subcooled droplet impacted

a highly thermally conductive spherical surface by theoretical and experimental method. The contact time of droplet decreased with increasing Weber number. Malgarinos et al. [25] used volume of fluid method to analyze the influence of size ratio of droplet to spherical particle. Two distinct regimes were identified: the partial/full rebound and the coating regimes. Liu et al. [29] released a droplet above the superhydrophobic surfaces textured with lattices of submillimetre-scale posts decorated with nanotextures. When the Weber number exceeded a critical value, the droplet bounced off the surface in a pancake shape without retraction, leading to a remarkable contact time reduction. The inclined surface is more ubiquitous in practical applications. It is demonstrated that the droplet impacting an inclined surface behaves asymmetry between the tangential and lateral direction along the surface, which can promote the droplet to rebound from the surface. Meanwhile, due to the tangential velocity, the droplet slides along the inclined surface, away from the impact position [31–33]. If two droplets impact an inclined surface successively, the off-center impact should be observed, which is different from horizontal surface and still poorly understood, especially on superhydrophobic surfaces. Thus, the process of two droplets impacting an inclined surface successively is worth to be investigated. As mentioned above, the impact velocity, the center-to-center distance, and the surface wettability have a significantly effect on the dynamic behaviors of two droplets. In this study, through lattice Boltzmann method, the effects of velocity ratio of two droplets and the length between the two impact points on the contact time are analyzed. The rebounding map at various surface wettability and velocity ratios is obtained as well.

2. Mathematical Model

2.1. Shan-Chen Lattice Boltzmann Model

In this study, a Shan-Chen lattice Boltzmann (LB) model is adopted, which is also called pseudopotential lattice Boltzmann model. The LB method is derived from the Boltzmann equation with the BGK approximation. The LB method simulates fluid flow by solving the discrete Boltzmann equation with a collision operator, such as the Bhatnagar-Gross-Krook (BGK) collision operator [34] and the multiple-relaxation-time (MRT) collision operator [35,36]. In the LB method, a discrete distribution function f_α is introduced to represent the fluid. With BGK collision operator, the distribution function satisfies the following Lattice Boltzmann equation [37]:

$$f_\alpha(\boldsymbol{x}+\boldsymbol{e}_\alpha\delta_t, t+\delta_t) = f_\alpha(\boldsymbol{x},t) - \frac{1}{\tau}\Big[f_\alpha(\boldsymbol{x},t) - f_\alpha^{\mathrm{eq}}(\boldsymbol{x},t)\Big] + \delta_t F'_\alpha(\boldsymbol{x},t) \tag{1}$$

where f_α $(\boldsymbol{x}, t)$ is the density distribution function, $\mathbf{e}_\alpha$ is the discrete velocity in the αth direction, δ_t is the time step, and $f_\alpha{}^{\mathrm{eq}}(\boldsymbol{x}, t)$ is the equilibrium distribution function. τ is a relaxation time, which is related to the kinematic viscosity by $\nu = c_s(\tau - 0.5)\ \delta_t$, where c_s is the sound speed. $F'_\alpha(\boldsymbol{x}, t)$ is the forcing term.

The LB equation is established with a collision-streaming theory, i.e., the LB equation can be split into two processes: the "collision" process [38]:

$$f_\alpha^*(\boldsymbol{x},t) = f_\alpha(\boldsymbol{x},t) - \frac{1}{\tau}\Big[f_\alpha(\boldsymbol{x},t) - f_\alpha^{\mathrm{eq}}(\boldsymbol{x},t)\Big] + \delta_t F'_\alpha(\boldsymbol{x},t) \tag{2}$$

and the "streaming" process:

$$f_\alpha(\boldsymbol{x}+\boldsymbol{e}_\alpha\delta_t, t+\delta_t) = f_\alpha^*(\boldsymbol{x},t) \tag{3}$$

The equilibrium distribution function $f_\alpha{}^{\mathrm{eq}}(\boldsymbol{x}, t)$ is given by,

$$f_\alpha^{\mathrm{eq}} = w_\alpha\rho\left[1 + \frac{\boldsymbol{e}_\alpha\cdot\boldsymbol{u}}{c_s^2} + \frac{(\boldsymbol{e}_\alpha\cdot\boldsymbol{u})^2}{2c_s^4} - \frac{\boldsymbol{u}\cdot\boldsymbol{u}}{2c_s^2}\right] \tag{4}$$

where w_α is the weight factor, and $\boldsymbol{u}$ is the macroscopic velocity. Equation (4) is derived from Maxwell's distribution function [39],

$$f = \frac{\rho}{2\pi/3}\exp(-\frac{3}{2}e^2)\exp(\frac{3}{2}(\boldsymbol{e}\cdot\boldsymbol{u}-u^2)\Big) \tag{5}$$

where $c^2 = \mathbf{c}\cdot\mathbf{c}$ and $u^2 = \boldsymbol{u}\cdot\boldsymbol{u}$. With Taylor series expansion for e^{-x}, the Equation (5) can be expanded around the stationary state as,

$$f = \frac{\rho}{2\pi/3}\mathrm{e}^{-\frac{3}{2}(c^2)}[1+3(\boldsymbol{c}\cdot\boldsymbol{u})-\frac{3}{2}u^2+\cdots] \tag{6}$$

A more general form of Equation (6) can be written as,

$$f_\alpha^{\mathrm{eq}} = \Phi w_\alpha\Big[A+B\boldsymbol{e}_\alpha\cdot\boldsymbol{u}+C(\boldsymbol{e}_\alpha\cdot\boldsymbol{u})^2+D\boldsymbol{u}\cdot\boldsymbol{u}\Big] \tag{7}$$

where A, B, C, and D are constants and are calculated based on the conservation principle (mass, momentum, and energy). Φ is scalar parameter, such as density, temperature, or species concentration. Then the Equation (4) can be obtained.

However, because the relaxation time τ is constant which determines the time from the initial status to next equilibrium status, the BGK scheme exists some drawbacks, i.e., the numerical instability, the limitation of the density ratio, and the viscosity dependence of the physical results. It has been founded that the MRT scheme has a better performance because the relaxation times in the MRT collision operator can be tuned individually. The basic method of MRT scheme is to use the transformation matrix $\boldsymbol{M}$ to achieve a multiple relaxation time [40–42],

$$f_\alpha(\boldsymbol{x}+\boldsymbol{e}_\alpha\delta_t, t+\delta_t) = f_\alpha(\boldsymbol{x},t)-(\boldsymbol{M}^{-1}\boldsymbol{\Lambda}\boldsymbol{M})_{\alpha\beta}\Big[f_\beta(\boldsymbol{x},t)-f_\beta^{\mathrm{eq}}(\boldsymbol{x},t)\Big]+\delta_t F'_\alpha(\boldsymbol{x},t) \tag{8}$$

$\boldsymbol{M}$ is an orthogonal transformation matrix, $\boldsymbol{\Lambda}$ is a diagonal matrix, and F'_α is the forcing term.

Using the orthogonal transformation matrix $\boldsymbol{M}$, the collision step of Equation (1) is obtained as follows

$$\boldsymbol{m}^* = \boldsymbol{m}-\boldsymbol{\Lambda}(\boldsymbol{m}-\boldsymbol{m}^{\mathrm{eq}})+\delta_t(\boldsymbol{I}-\frac{\boldsymbol{\Lambda}}{2})\boldsymbol{S} \tag{9}$$

where $\boldsymbol{I}$ is the unit tensor, $\boldsymbol{m} = \boldsymbol{M}\boldsymbol{f}$, $\boldsymbol{m}^{\mathrm{eq}} = \boldsymbol{M}\boldsymbol{f}^{\mathrm{eq}}$. The equilibrium distribution function $\boldsymbol{m}^{\mathrm{eq}}$ in the moment space is given by,

$$\begin{aligned}\boldsymbol{m}^{eq} = \rho(1,-11+19(u_x^2+u_y^2+u_z^2),3-\tfrac{11}{2}(u_x^2+u_y^2+u_z^2),u_x,-\tfrac{2}{3}u_x,u_y,-\tfrac{2}{3}u_y,u_z,-\tfrac{2}{3}u_z,\\ 2u_x^2-u_y^2-u_z^2,-\tfrac{1}{2}(2u_x^2-u_y^2-u_z^2),u_y^2-u_z^2,-\tfrac{1}{2}(u_y^2-u_z^2),u_xu_y,u_yu_z,u_xu_z,0,0,0)^T\end{aligned} \tag{10}$$

where u_x, u_y and u_z are fluid velocity components along the $x-$, $y-$, and z direction, respectively. $\boldsymbol{S}$ is an improved forcing term proposed by Li et al. [43], which represents the molecular interactions that cause phase segregation and is employed to achieve thermodynamic consistency,

$$\begin{aligned}\boldsymbol{S} = (0,38(u_xF_x+u_yF_y+u_zF_z)+\tfrac{114\varepsilon(F_x^2+F_y^2+F_z^2)}{\psi^2\delta_t(1/s_2-0.5)},-11(u_xF_x+u_yF_y+u_zF_z),\\ F_x,-\tfrac{2}{3}F_x,F_y,-\tfrac{2}{3}F_y,F_z,-\tfrac{2}{3}F_z,4u_xF_x-2u_yF_y-2u_zF_z,-2u_xF_x+u_yF_y+u_zF_z,2u_yF_y-2u_zF_z,\\ -u_yF_y+u_zF_z,u_xF_y+u_yF_x,u_yF_z+u_zF_y,u_xF_z+u_zF_x,0,0,0)^T\end{aligned} \tag{11}$$

where ψ is the effective mass, ε is used to ensure the mechanical stability.

The total force $\boldsymbol{F}$ consists of $\boldsymbol{F}_\mathrm{f}$, $\boldsymbol{F}_\mathrm{s}$, and $\boldsymbol{F}_\mathrm{b}$, which represents the fluid-fluid interaction force, the fluid-solid interaction force, and the body force, respectively [38],

$$\boldsymbol{F}_f(\boldsymbol{x},t) = -G\psi(\boldsymbol{x},t)\sum_{\alpha=0}^{18}w_\alpha\psi(\boldsymbol{x}+\boldsymbol{e}_\alpha\delta_t,t)\boldsymbol{e}_\alpha \tag{12}$$

$$\boldsymbol{F}_s(\boldsymbol{x},t) = -G_{ads}\psi(\boldsymbol{x},t)\sum_{\alpha=0}^{18} w_\alpha \psi(\boldsymbol{x},t)s(\boldsymbol{x}+\boldsymbol{e}_\alpha\delta_t,t)\boldsymbol{e}_\alpha \tag{13}$$

$$\boldsymbol{F}_b(\boldsymbol{x},t) = \rho(\boldsymbol{x},t)g \tag{14}$$

where g is the gravitational acceleration, G is the parameter which determines the fluid strength, s is an indicator function which equals to 1 or 0 for solid or fluid nodes respectively, and the various contact angles are achieved by G_{ads}. The macroscopic density ρ and velocity $\mathbf{u}$ are obtained from,

$$\rho = \sum_{\alpha=0}^{18} f_\alpha; \rho\boldsymbol{u} = \sum_{\alpha=0}^{18} \boldsymbol{e}_\alpha f_\alpha + \frac{\delta_t}{2}\boldsymbol{F} \tag{15}$$

The effective mass ψ can be computed as,

$$\psi(\boldsymbol{x}) = \sqrt{\frac{2(p-\rho c_s^2)}{Gc_s^2}} \tag{16}$$

To achieve large liquid-gas density ratio and guarantee the numerical stability and accuracy, the C-S equation of state is chosen, which is derived by modifying the repulsive term of the van der Waals EOS [44],

$$p = \rho RT\frac{1+b\rho/4+(b\rho/4)^2-(b\rho/4)^3}{(1-b\rho/4)^3} - a\rho^2 \tag{17}$$

where G represents the interaction strength of the fluid, $a = 0.4963(RT_c)^2/p_c$, $b = 0.18727RT_c/p_c$, T_c and p_c are the critical temperature and pressure, respectively. In this paper, the parameters are set to be $a = 0.25$ lu^5 (mu ts^2)$^{-1}$, $b = 4$ lu^3 mu^{-1}, and $R = 1$ lu^2 (ts^2 tu) $^{-1}$, which provide a large density ratio, a sharp interface, and maintain numerical stability. The liquid density $\rho_l = 0.455$ mu lu^{-3} and the vapor density $\rho_g = 0.000606$ mu lu^{-3}, corresponding to $T = 0.5T_c$. The surface tension is $\sigma = 0.007698$ mu ts^{-2}. Here, mu denotes the mass unit and ts denotes the time step.

2.2. Model validation

Numerical simulations are conducted to validate the capability of lattice Boltzmann model for investigating the dynamic behavior of droplet impact. In the kinematic phase of impact, the shape of the droplet resembles a truncated sphere, and no spreading lamella is yet visible [45]. This phase is observed only at $\tau^* << 1$, where $\tau^* = v_0 t/D_0$. It is demonstrated that in the kinematic phase, the dimensionless spreading factor $D^* = D/D_0$ is proportional to $(\tau^*)^{0.5}$, and the theoretical analysis indicates a coefficient 2.0 [46,47]. Here, D is the spreading diameter during the impact. Moreover, D^* in this phase is independent of the droplet physical properties and the surface wettability. Thus, a superhydrophobic surface with contact angle $\theta_0 = 157°$ is considered. The droplet just touches the surface and impacts with various velocities, while the initial diameter, surface tension, and the kinematic viscosity is kept constant as 60 lu (lattice units), $\sigma = 0.007698$ mu ts^{-2}, and 0.0167 mu^2 ts^{-1}, respectively. The spreading diameters within $\tau^* < 0.1$ is recorded, thus D^* in the kinematic phase at various *We* and corresponding Reynolds number ($Re = \rho_l v_0 D_0/\mu_l$, where μ_l the dynamic viscosity) is obtained. As shown in Figure 1a, a curve fit between D^* and $(\tau^*)^{0.5}$ is presented with the coefficient 2.08, which is consistent with the theoretical results.

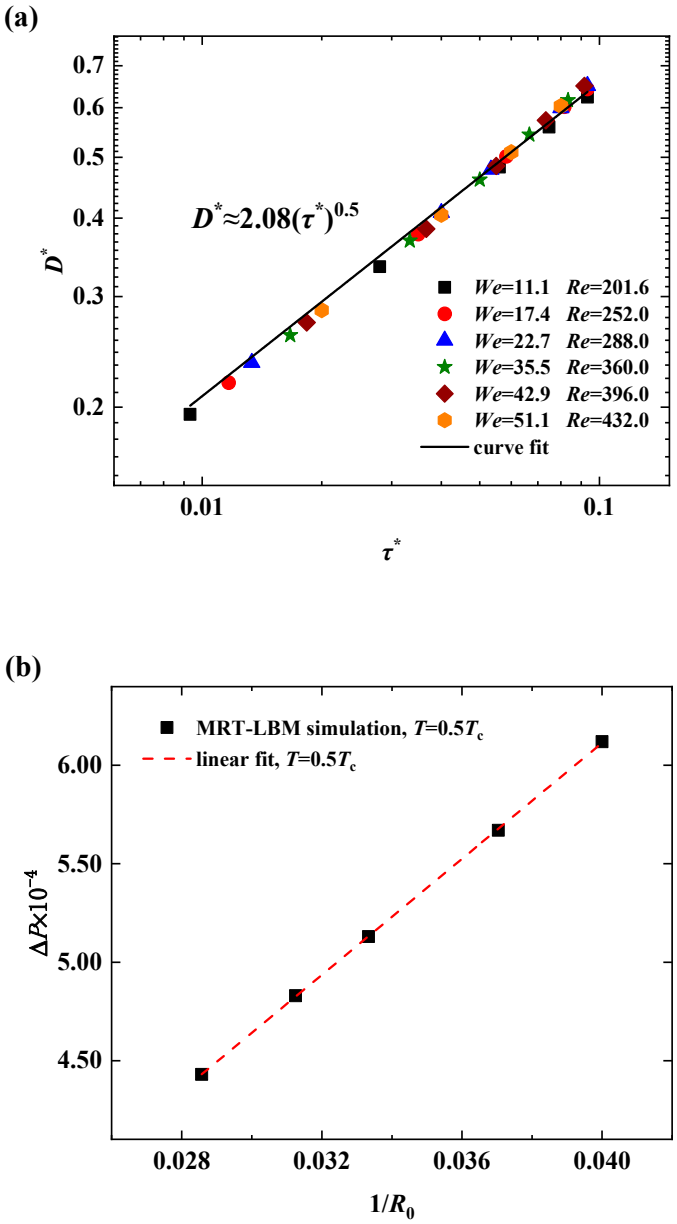

Figure 1. The model validation (**a**) Time evolution of the dimensionless spreading factor in the kinematic phase for six different cases; (**b**) The Laplace law.

Considering a stationary spherical droplet placed at the center of a square domain, the Laplace law is given by:

$$\Delta p = p_{\text{in}} - p_{\text{out}} = \frac{2\sigma}{R_0} \tag{18}$$

where Δp is the pressure difference across the interface of the droplet, p_{in} and p_{out} are the pressures inside and outside the droplet, R_0 is the radius of the leading droplet. As plotted in Figure 1b, the pressure difference Δp linearly depends on $1/R_0$, and the slope of the fitted line equals to 0.01540, which corresponds to a surface tension of 0.007698 mu ts^{-2}.

2.3. The Simulation Setup

As depicted in Figure 2, two identical droplets successively impact a smooth surface placed obliquely with an angle of inclination α. As a starting point to investigate the dynamic behaviour of two droplets successively impacting an inclined surface, a typical angle of inclination 45° is just chosen.

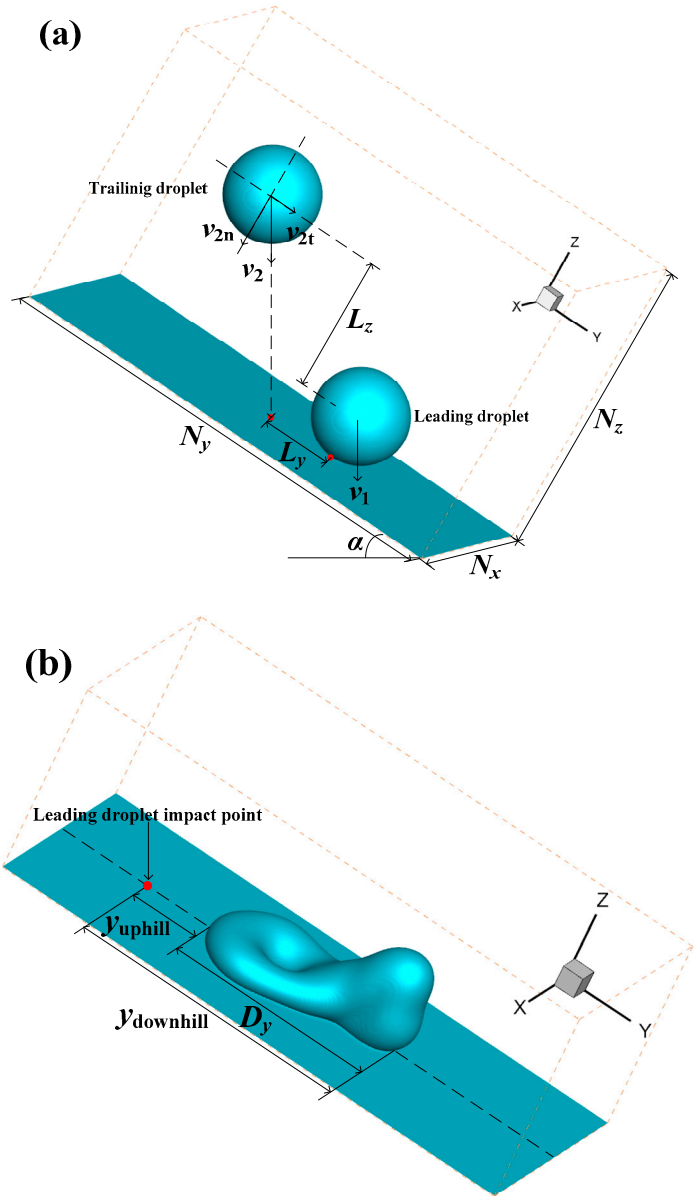

Figure 2. Schematic of two droplets impacting an inclined surface successively (**a**) The initial state of two droplets; (**b**) The morphology of two droplets during spreading and retraction process.

To facilitate the simulation, a Cartesian coordinate system is defined with its x, y, and z axes pointing to the direction along the lateral, tangential, and perpendicular to the inclined surface, respectively. The leading droplet just touches the surface, and the trailing droplet above the surface in a distance. The two red points represent the impact positions of two droplets separately, and the length of the impact points along the y direction is defines as L_y. When the impact point of trailing droplet is behind that of leading droplet, $L_y > 0$, otherwise $L_y < 0$, and $L_y = 0$ means that the two droplets have the same impact point. The center of the two droplets along the x direction falls the same line. The center-to-center distance between the two droplets along the z direction is defined as L_z. The diameters of the droplets are $D_0 = 60$ lu. The normal velocity of the leading droplet is defined as v_{1n} and kept constant. The normal velocity of the trailing droplet is v_{2n}, and the ratio of normal velocity of the trailing to leading droplet is v_r, i.e., $v_r = v_{2n}/v_{1n}$. In the impact process, the length between the uphill contact point and leading droplet impact point is referred to y_{uphill}, and $y_{downhill}$ is defined in the same way. The length between the uphill contact point and downhill contact point is D_y. The droplet diameter and the normal velocity of the leading droplet are chosen to be the characteristic

length and velocity. Thus, all the length parameters can be nondimensionalized by $L_y^* = L_y/D_0$, $L_z^* = L_z/D_0$, $y_{\text{uphill}}^* = y_{\text{uphill}}/D_0$, $y_{\text{downhill}}^* = y_{\text{downhill}}/D_0$, $D_y^* = D_y/D_0$, respectively. In this paper, the normal Weber number is fixed at $We_n = \rho D_0 v_{1n}^2/\sigma = 22.7$. No slip boundary condition is applied to the solid surface, and periodic boundary condition is executed on the sides of the domain. It should be noted that the quantities in our simulations are based on the lattice units.

3. Results and Discussion

As indicated in Table 1, the dynamic behaviors of two successive droplets impacting an inclined surface are investigated at various L_y^*, L_z^*, v_r, and θ_0. It should be emphasized that only the situations of two droplets coalescence are investigated in this work. In Section 3.1, the effect of velocity ratio (v_r = 0.7~1.5) on the contact time is explored under the condition that $\theta_0 = 157°$, $L_y^* = 0$, and L_z^* are fixed at 0.83, 1.0, 1.18, 1.33, 1.5, respectively. In Section 3.2, the rebounding map at various v_r and θ_0 is depicted, where $L_y^* = 0$ and $L_z^* = 1.18$. In Section 3.3, the effect of length of impact points (L_y^* = −2.5~1.0) on the contact time is studied, where the L_z^*, v_r, and θ_0 are fixed at $L_z^* = 1.18$, $v_r = 1.0$, and θ_0 = 157°, respectively.

Table 1. The cases for two successive droplets impacting an inclined surface in the present study.

Case	L_y^*	L_z^*	v_r	θ_0
Section 3.1	0	0.83	0.7~1.5	157°
Section 3.1	0	1.0	0.7~1.5	157°
Section 3.1	0	1.18	0.7~1.5	157°
Section 3.1	0	1.33	0.7~1.5	157°
Section 3.1	0	1.5	0.8~1.5	157°
Section 3.2	0	1.18	0.7~1.5	120°~157°
Section 3.3	−2.5~1	1.18	1.0	157°

As a typical situation, the mass conservation at each time step was checked when two droplets successively impact the 45° inclined surface at the same impact point with $v_r = 1.0$ and $L_z^* = 1.18$. The ratio of the total mass at each time step to the initial total mass was calculated, so was the mass of two droplets. The ratio of the total mass is always equal to 100%, which means the total mass is conservative. The ratio of the mass of two droplets exists a little fluctuation, but the maximum deviation is within 2.85%, which is acceptable for numerical simulation.

3.1. Effect of Velocity Ratio on Contact Time

The evolutions of the two successive droplets impacting the surface with $v_r = 0.7$ and 1.5 are illustrated in Figures 3 and 4, respectively. The first line is from the front view, and the second line is from the top view. It should be noted that the contact time in this work is from the leading droplet touching the surface until both droplets bounce off the surface. The contact time is nondimensionalized as $t_c^* = t_c/(\rho R_0^3/\sigma)^{1/2}$ with an inertia-capillarity scale.

As shown in Figure 3, the leading droplet first spreads along the inclined surface, and the center remains spherical with a rim formed at the droplet periphery in the initial of spreading (Figure 3a). When the leading droplet spreads to the maximum extent, the thickness of film center is lower than the rim. Approximatively, the whole liquid film remains circular due to the unapparent asymmetry. The trailing droplet approaches the leading droplet constantly, but the two droplets still do not touch each other, owing to the lower velocity of trailing droplet (Figure 3b). The asymmetry of the leading droplet emerges prominently in the recoiling stage, and the retraction becomes standing out in the *x*-direction. Meanwhile the thickness of liquid film gets increasing, and a torus is formed without any liquid in the center, which is called dry-out [48]. As the leading droplet slides along the surface, it is away from the impact point gradually. So the trailing droplet lands on the surface entirely, and it connects with the leading droplet through a slender liquid bridge (Figure 3c). With the liquid bridge

growing up rapidly, the upper border of the leading droplet starts coalescing with the lower border of the trailing droplet, however the residual parts of the two droplets get affected scarcely. The leading droplet continues recoiling along the x-direction, resulting in the whole droplet raising up gradually, while the trailing droplet remains its spreading process with a rim formed (Figure 3d). The desynchrony of the dynamic leads a weak interaction effect between two droplets, despite the fact that two droplets slide along the surface integrally. When the spreading of the trailing droplet reaches its maximum, the leading droplet undertakes recoiling and lifting (Figure 3e). While the leading droplet finishes its retraction along the x-direction, the recoiling along the y-direction continues with the droplet lifting up constantly. The trailing droplet retracts along the x-direction primarily and raises up gradually (Figure 3f–h). At the later period of recoiling stage, an air layer appears close to the wall of the leading droplet between the two droplets, and the leading droplet bounces off the surface firstly, resulting in a decrease in contact area between the trailing droplet and the surface. The process of the trailing droplet bouncing off the surface is promoted (Figure 3i). Ultimately, the trailing droplet bounces off the surface due to the retraction as well as the lifting by leading droplet (Figure 3j). The coalescence of the two droplets during the impact process has barely influence on the dynamic behavior, which is ascribed to the motions of two droplets keeping relative independence.

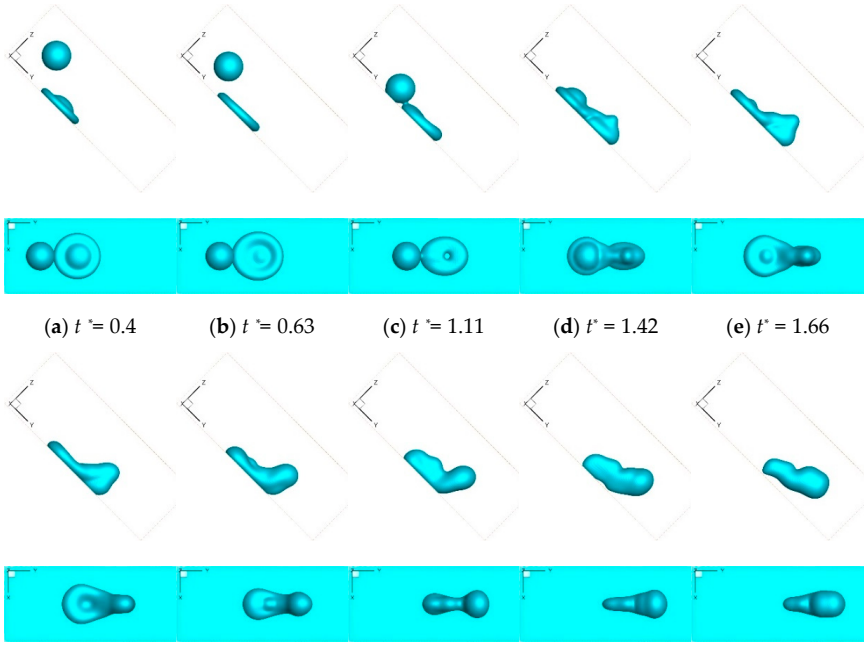

(**a**) t^* = 0.4 (**b**) t^* = 0.63 (**c**) t^* = 1.11 (**d**) t^* = 1.42 (**e**) t^* = 1.66

(**f**) t^* = 1.9 (**g**) t^* = 2.22 (**h**) t^* = 2.53 (**i**) t^* = 2.93 (**j**) t^* = 3.17

Figure 3. Snapshots of two successive droplets impacting an inclined superhydrophobic surface at v_r = 0.7 and $L_z{}^*$ = 1.18.

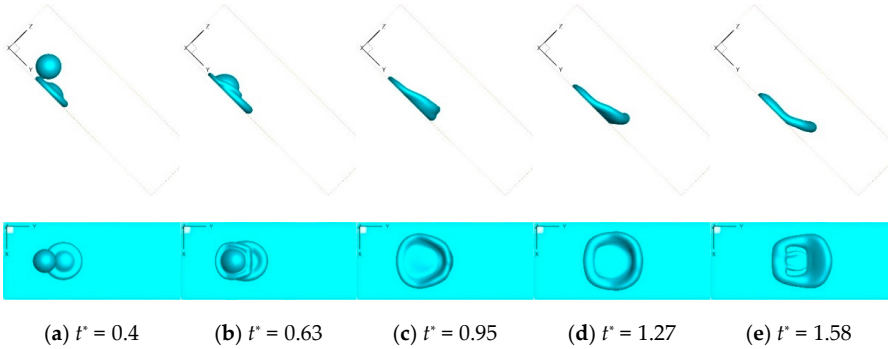

(**a**) t^* = 0.4 (**b**) t^* = 0.63 (**c**) t^* = 0.95 (**d**) t^* = 1.27 (**e**) t^* = 1.58

Figure 4. *Cont.*

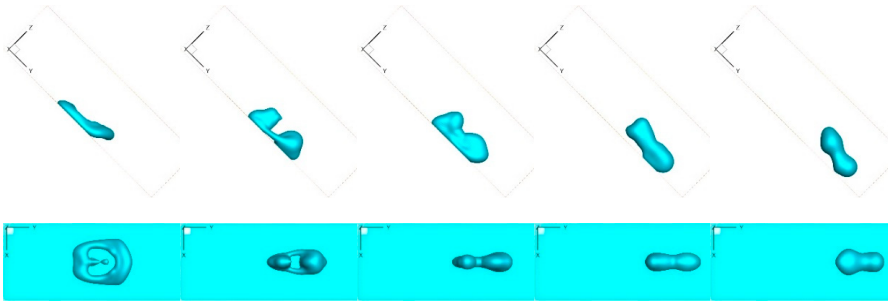

(**f**) t^* = 1.82 (**g**) t^* = 2.53 (**h**) t^* = 2.85 (**i**) t^* = 3.32 (**j**) t^* = 3.8

Figure 4. Snapshots of two successive droplets impacting an inclined superhydrophobic surface at v_r = 1.5 and L_z^* = 1.18.

Figure 4 shows the snapshots of the two droplets successively impacting the superhydrophobic surface with v_r = 1.5. On account of the same impact velocity of the leading droplet, the initial spreading is exhibited similarly with that in Figure 3a. The trailing droplet gets in touch with the leading one much earlier due to the higher velocity, with a part of it landing on the liquid film of the leading droplet, and the other part falling on the surface (Figure 4a). Thereafter, a thorough coalescence of the two droplets is observed because the trailing droplet crushes into the former liquid film at a high velocity. Meanwhile a plenty of liquid is pushed into the periphery of the liquid film of the leading droplet, which forces the film to keep spreading along the x-direction. As a result, the liquid pushed downhill catches up with the liquid film of the leading droplet (Figure 4b,c). The spreading velocity exceeds the motion of contact line due to the abrupt increase of downhill liquid, so that the liquid film starts to extend upwards. The central liquid of the film continues to diffuse, forming a thick rim relatively, and simultaneously the liquid film reaches its maximum in the x-direction (Figure 4d). As the uprising film keeps extend upwards, the liquid film turns to recoil in the x-direction, then the central liquid ruptures. This is because that the center liquid is pumped to the periphery by the trailing droplet (Figure 4e). The drag force generated by the liquid sliding on the surface of the droplet gradually causes a velocity reduction of the liquid film in the air, which leads to a bend tendency. Along with the motion of the contact line, the liquid film on the surface goes downhill continually, which makes the distance between the film in the air and on the surface decrease. At this point, the liquid film keeps its recoiling in the x-direction, and the rupture of central film gets intensified (Figure 4f). Two retraction points of the ruptured film emerged along the y-direction. The downhill liquid film catches up with the film in the air ultimately, then coalesces and retracts together into a larger droplet, and the uphill liquid film on the surface retracts into another droplet independently. The two droplets are linked by two slender liquid bridges at two sides (Figure 4g). As the two droplets recoil along the x-direction, a coalesced droplet gets formed finally (Figure 4h). The new liquid bridge keeps growing after the coalescence, which causes an air layer to arise close to the uphill of the coalesced droplet. The uphill part of the coalesced droplet finishes its retraction along the x-direction primarily due to the smaller size, then bounces off the surface firstly. After a period of time, the downhill part detaches from the surface slowly (Figure 4i,j).

Comparing Figures 3 and 4, the most obvious difference is, at higher velocity ratio vr, the downhill liquid spreading in the air which retouches the surface in the retraction process, while it is not seen at lower velocity ratio. In this study, the rebounding processes in Figures 3 and 4 are defined as regime 1, and regime 2, respectively. Figure 5a plots the map for rebounding regime of two successive droplets impacting with various v_r and L_z^*. The solid symbols represent regime 1, and the empty symbols represent regime 2. When L_z^* = 1.33 or 1.5, there exists only regime 1 because of the long distance along the z direction. Reducing the L_z^*, in case that the v_r exceeds the critical value, the rebounding regime turns from regime 1 to regime 2. The critical value of v_r reduces at a smaller L_z^*. In other words, the two successive droplets are more likely to rebound from the surface in regime 2, if the two droplets

get closer. Figure 5b shows the coalescence time t_1^* of two droplets at various v_r and L_z^*. The dashed line represents the time that the leading droplet reaches the maximum spreading in the lateral direction. The regime 2 is observed only in the situation that the coalescence time t_1^* of two droplets is smaller than the time that the leading droplet reaches the maximum spreading in the lateral direction, i.e., the two droplets coalesce in the spreading process of the leading droplet.

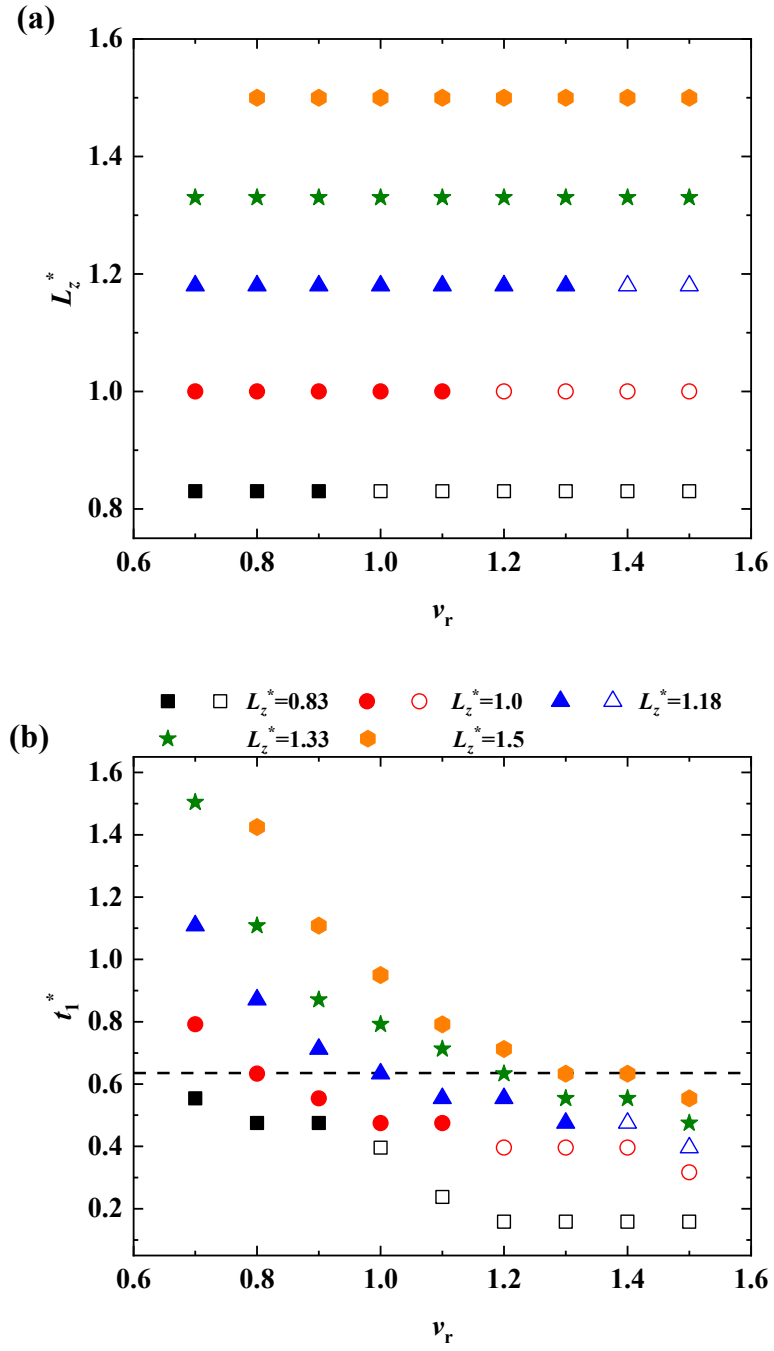

Figure 5. (**a**) Map for rebounding regime of two successive impacting droplets with various v_r and L_z^*; (**b**) Variation of coalescence time t_1^* of two droplets for v_r at various L_z^*.

The contact time of two successive droplets impacting an inclined superhydrophobic surface as a function of v_r at various L_z^* is presented in Figure 6. For different L_z^*, if the droplets leave the surface in regime 1, as the velocity ratio increases, the contact time increases slightly or fluctuates in small range. Though the contact time is relative stable, the morphologies at the detaching moment

at various velocity ratios are different, as shown in Figure 7. When v_r = 0.7, the two droplets spread and retract respectively, and the leading one bounces off first, promoting the trailing droplet to detach, and the coalesced droplet in elongated shape along the *y*-direction (Figure 7a). As the velocity ratio up to v_r = 1.0, a complete coalescence is exhibited, causing an integral droplet to bounce off the surface (Figure 7b). With the velocity ratio increasing, more liquid flows into the front part of the droplet, so that the bending droplet gets pressed close to the surface at the bouncing moment (Figure 7c,d). If the velocity ratio exceeds the critical value, the bouncing model turns to regime 2, and the contact time gets a sharp increase. With smaller L_z^*, the increment of contact time is more obvious. In regime 2, owing to the retouching of the front part of the droplet, the rear of the droplet detaches from the surface first, then the front part leaves the surface gradually (Figure 4j).

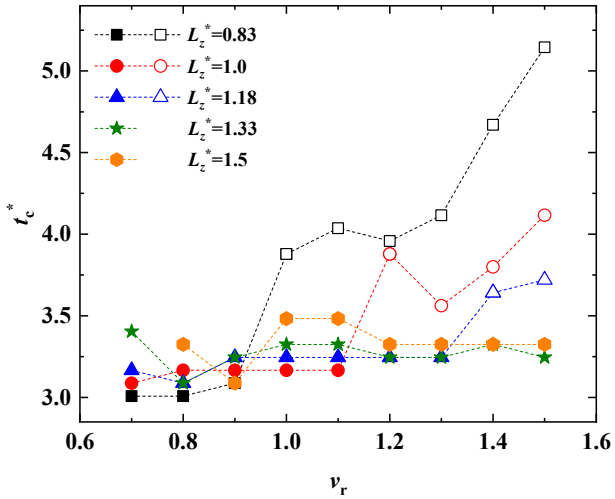

Figure 6. Contact time of two successive droplets with various droplet ratios and L_z^*.

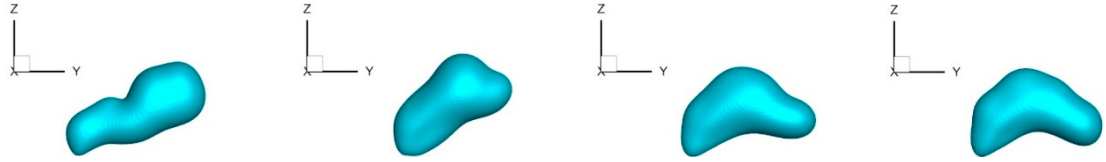

(**a**) v_r = 0.7 (**b**) v_r = 1.0 (**c**) v_r = 1.2 (**d**) v_r = 1.3

Figure 7. The different morphology of droplet rebounding from the surface with various velocity ratios at L_z^* = 1.18.

To explain the difference of contact time with various velocity ratios, Figure 8 depicts the time evolution of the characteristic length y_{uphill}^*, $y_{downhill}^*$ and D_y^* at v_r = 0.7, 1.0, 1.5. The solid symbols represent y_{uphill}^*, and the hollow symbols represent the parameter $y_{downhill}^*$. In the spreading stage, two curves coincide at different velocity ratios for the reason that the velocity of leading droplet remains constant, as plotted in Figure 8a. When the two droplets connect each other, the y_{uphill}^* declines sharply, whereas the $y_{downhill}^*$ keeps its initial trend. The y_{uphill}^* turns to grow up after reaching a minimum. With higher velocity ratios, the increasing rate is larger due to the larger kinetic energy. As a result, the uphill of the droplet moves more rapidly. The $y_{downhill}^*$ increases synchronously with y_{uphill}^* at v_r = 0.7, then it reaches a maximum and starts to reduce slowly. When the leading droplet bounces off the surface, the $y_{downhill}^*$ decreases sharply, which causes a conspicuous de-wetting. Ultimately, the coalesced droplet detaches from the surface, leading to the shortest contact time (Figure 3i). Even though the increasing rate of y_{uphill}^* is the largest at v_r = 1.5, the $y_{downhill}^*$ performs a reducing tendency at first, then growing up rapidly afterwards. This is because the liquid film of leading droplet starts to spread upwards because of the significant inertia force of the trailing droplet, meanwhile

the central film gets ruptured. As a result, the $y_{downhill}^*$ decreases temporarily (Figure 4d–f). When the spreading liquid film in the air falls down and retouches the surface (Figure 4g), the $y_{downhill}^*$ increases immediately. The de-wetting process scarcely appears as $y_{downhill}^*$ keeps growing up. As the rear of the coalesced droplet bounces off, the y_{uphill}^* increases rapidly. When the coalesced droplet detaches the surface gradually, the y_{uphill}^* and $y_{downhill}^*$ meet each other. The coalesced droplet dewets first and then wets surface again, which is responsible for the contact time increasing by a large margin (Figure 4i). In contrast, the y_{uphill}^* grows up stably at v_r = 1.0, and the $y_{downhill}^*$ increases slightly after $t^* > 2.0$, which performs a mild process of dewetting. The similar evolutions are demonstrated when v_r ranged from 0.9 to 1.3, resulting in a constant contact time relatively. The evolution of D_y^* with various v_r is shown in Figure 8b. The D_y^* stays consistent at the early spreading stage despite the various velocity ratios. Thereafter, the D_y^* gets a significant increase successively, corresponding the two droplets connect each other, and the part of the trailing droplet falls on the surface, resulting in the increase of D_y^*. The D_y^* increases the most at v_r = 0.7, it is because that the leading droplet undergoes the recoiling process at this moment, and it is can be seen that D_y^* decreases obviously before the explosion occurs. Comparing the D_y^* at v_r = 0.7 and 1.0, after the coalesced droplet reaches the maximum spreading, a same rate of declining of the D_y^* is performed at early stage. Then the D_y^* decreases sharply and the coalesced droplet bounces off promptly at v_r = 0.7. Whereas, the D_y^* reduces slowly down at v_r = 1.0, because of the $y_{downhill}^*$ increases slightly. With v_r = 1.5, two peak values of D_y^* are observed, which lengthen the contact time significantly.

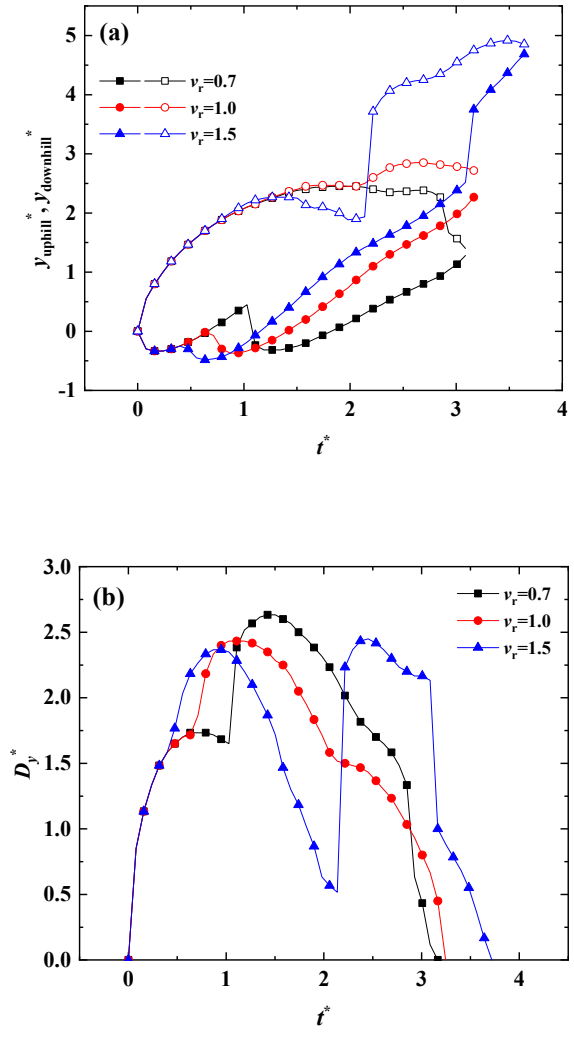

Figure 8. The evolutions of (**a**) y_{uphill}^*, $y_{downhill}^*$, and (**b**) D_y^* with various velocity ratios at L_z^* = 1.18.

3.2. Outcome Map of Rebounding

As mentioned in Section 3.1, when two successive droplets impact a superhydrophobic surface, increasing the velocity ratio causes the rebounding turning from regime 1 to regime 2, and the contact time increases sharply. Therefore, the coalesced droplet may not rebound when the surface hydrophobicity is decreased, and the velocity ratio increases until exceed a threshold. In this section, whether the coalesced droplet rebounds or not after two successive droplets impacting with various velocity ratios and surface hydrophobicity is explored. The L_y^* is fixed at 0, and L_z^* is set to be 1.18.

Figure 9 shows the outcomes of two successive droplets impacting with various velocity ratios and the surface with various contact angles. When the contact angle is 157°, the coalesced droplets rebound at all velocity ratios. If the contact angle is equal to 150°, coalesced droplets still rebound at most of velocity ratios, only the two successive droplets impacting with v_r = 1.5 cannot rebound. When the contact angle reduces to 140°, the coalesced droplets cannot rebound in a larger velocity ratio range which expands to 1.3. For the contact angle is 130°, the coalesced droplets with velocity ratio larger than 1.1 cannot rebound. Until the contact angle is 120°, the coalesced droplets cannot rebound at all cases.

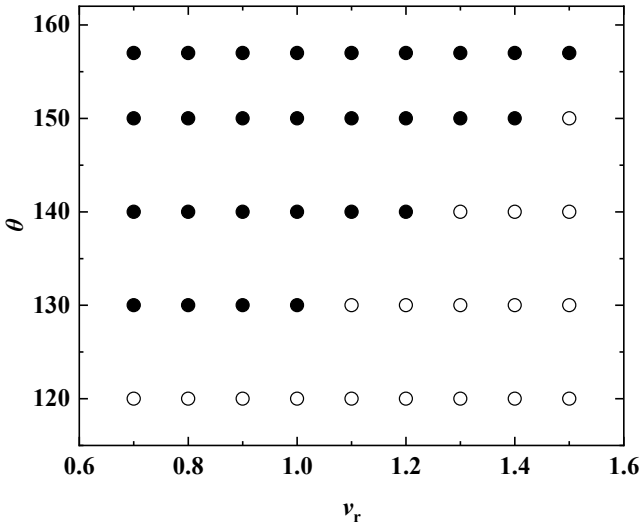

Figure 9. Map for outcomes of two successive droplets impacting with various velocity ratios and the surface with various contact angles. The solid symbols represent that the coalesced droplets rebound from the surface, whereas the empty ones are not.

Figure 10 shows the morphology evolution of two successive droplets impacting an inclined surface with θ = 140° at v_r = 1.5. Comparing with the impact process on superhydrophobic surface in Figure 4, the dynamic behavior in the spreading stage is similar (Figure 10a–c). Two successive droplets come into contact at the same moment as in Figure 4, then quickly merge. Subsequently, the lateral spreading reaches its maximum, while the downhill of the liquid film extends into the air continuously. However, the differences in the retraction process are more obvious between Figures 4 and 10. First, on the surface with contact angle of 140°, when the lateral spreading reaches its maximum, the rupture is observed at the inner corners of the liquid film, resulting in the aggravated rupture of the center of the liquid film (Figure 10c,d). Second, comparing Figures 10e and 4g, at the same moment, it is found that the liquid film on the hydrophobic surface retracts less, and the entire film is longer both along the x and y directions than that on the superhydrophobic surface, the film height is shorter as well. Third, in spite of the fact the air layer also appears near the uphill between the two droplets, but because of the strong adhesion of the surface, the air film cannot extend after it has grown to a certain extent (Figure 10f,g). Under the suppression of the uphill liquid, the air film disappeared, without rebound behavior as shown in Figure 4i (Figure 10h). After that, the coalesced droplet retracts rapidly

along the y direction, at last the coalesced droplet has been sliding along the inclined surface after several oscillations along the x and y directions (Figure 10i,j).

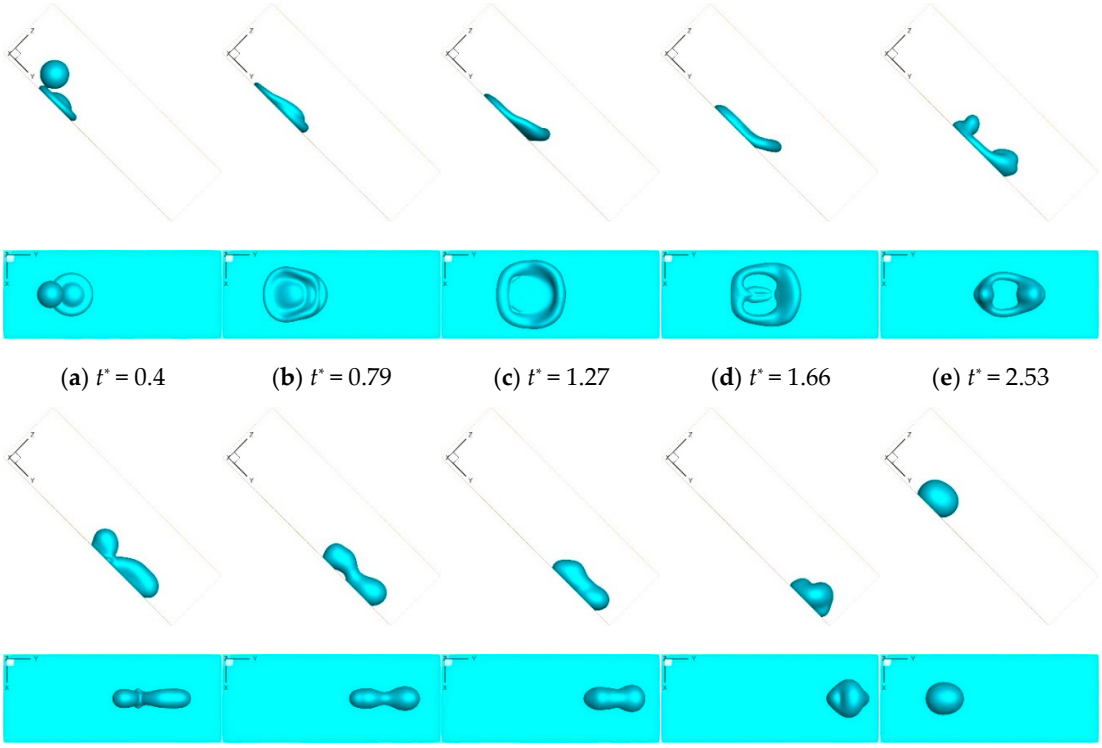

(**a**) $t^* = 0.4$ (**b**) $t^* = 0.79$ (**c**) $t^* = 1.27$ (**d**) $t^* = 1.66$ (**e**) $t^* = 2.53$

(**f**) $t^* = 3.32$ (**g**) $t^* = 4.12$ (**h**) $t^* = 4.75$ (**i**) $t^* = 5.7$ (**j**) $t^* = 14.41$

Figure 10. Snapshots of two successive droplets impacting an inclined surface with $\theta = 140°$ at $v_r = 1.5$.

Figure 11 compares the velocity fields when the air film is generated at $v_r = 1.5$, with contact angle of 140° and 157°, respectively. When the contact angle is 140°, it can be seen that a small upward velocity emerges at the air film, and the velocity direction at the rear of the coalesced droplet is almost parallel to the surface. The velocity at air film is suppressed which causes the upward velocity and air film to disappear. When the contact angle is 157°, the upward velocity also appears at air film, but it is larger than that of 140°. Furthermore, there is an upward component of the velocity at the rear of the coalesced droplet, leading to the range of the air film expanding continuously.

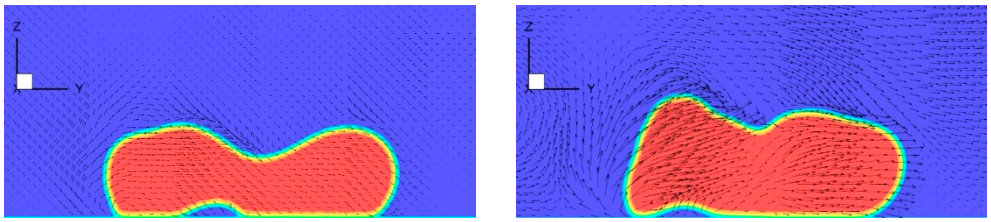

(**a**) $\theta = 140°$ (**b**) $\theta = 157°$

Figure 11. The different velocity field of droplet between $\theta = 140°$ and $\theta = 157°$ at $v_r = 1.5$.

3.3. Effect of Length Between Impact Points on Contact Time

The length between the impact points also affects the coalescence of two droplets, and then influences the contact time ultimately. In this section, the effect of the length of the impact points L_y* on the contact time is investigated.

Figure 12 shows the contact time of two successive droplets impacting inclined surfaces as a function of L_y*. The morphologies of the two droplets at the connecting and rebounding moment

with various L_y* are presented in Figure 13. At L_y* = −0.67, the contact time reaches a maximum, and decreases when the length L_y* declined to −2.5 or raised to 1. For L_y* < −2 and L_y* > 0.33, the majority of the trailing droplet falls on the surface due to the larger length between two droplets. The trailing droplet lands at the front of the leading one at L_y* < −2, and an opposite direction occurs at L_y* > 0.33. In this range of L_y*, each droplet spreads and retracts separately, then the leading droplet bounces off and lifts the trailing one to detach from the surface (Figure 13a,d). As a result, the coalesced droplet rebounds in an elongated shape and the contact time is short. If L_y* = −1.83 or varies in the range of −0.5~0.17, more liquid of the trailing droplet lands on the leading one at the connecting moment, making a stronger coalescence. Hence the contact time increases (Figure 13c). As L_y* varies in the range from −1.67 to −0.67, the coalescence becomes stronger further, even the whole trailing droplet falling on the leading one. Then an integrated droplet detaches from the surface (Figure 13b), and the contact time increases further.

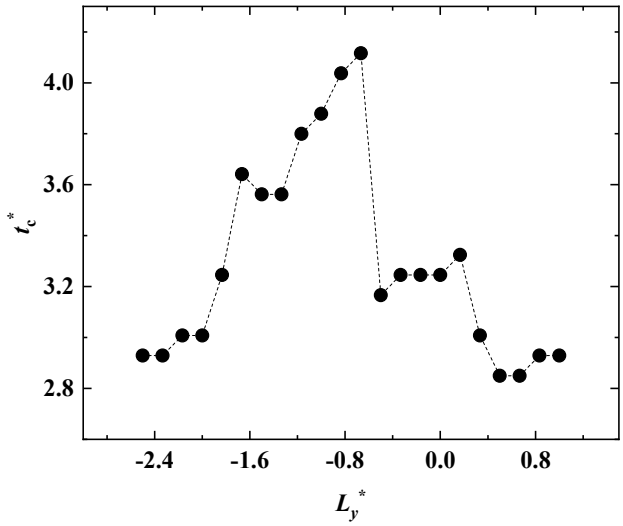

Figure 12. The contact time versus L_y*.

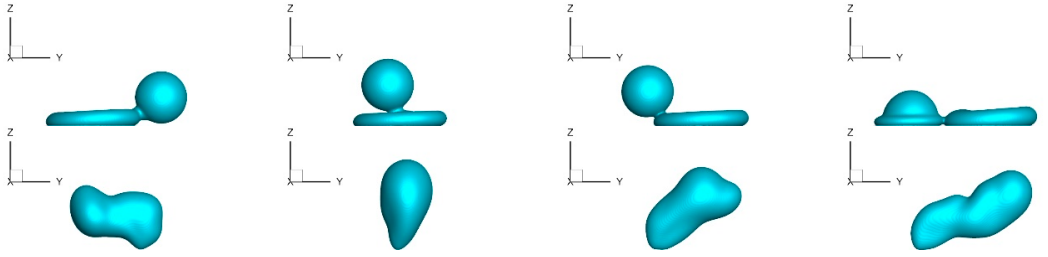

Figure 13. The different droplet morphology at various L_y*. The first line is the moment that two droplets connect, and the second line is the moment that they rebound from the surface.

Figure 14 plots the evolution of y_{uphill}*, $y_{downhill}$* and D_y* with various lengths between the impact points L_y*. The solid symbols represent y_{uphill}*, and the hollow symbols represent $y_{downhill}$* in Figure 14a. The curves which depict y_{uphill}* are coincided with each other at different L_y* in the spreading stage, so do $y_{downhill}$*. Once the trailing droplet touches the surface, different tendencies are exhibited. At L_y* = −2.33, the trailing droplet lands in front of the leading one and part of the trailing droplet lands on the surface, resulting in a sharp increasing of $y_{downhill}$*, meanwhile y_{uphill}* remains constant. Because of the larger length between the two impact points, each droplet spreads and retracts separately. As a result, the leading droplet bounces off the surface promptly at the end of the retracting phase. So that y_{uphill}* grows up rapidly. In the meantime, $y_{downhill}$* reaches a maximum, then decreases at a low rate. The two curves get intersected which represents the coalesced droplet detaching from the surface

(Figure 13a). Analogously, the spreading and retraction are relatively independent of each droplet at $L_y^* = 0.67$ except that the trailing droplet falls at the rear of the leading droplet (Figure 13d). So that y_{uphill}^* reduces rapidly, while $y_{downhill}^*$ keeps constant. Once the leading droplet bounces from the surface firstly, y_{uphill}^* raises up at a constant rate, and the $y_{downhill}^*$ decreases sharply. Then, the two curves intersect. The contact time is quite short in both cases above, because the interaction between two droplets is relatively weak. The details of the evolution of $L_y^* = 0$ are discussed in Section 3.1. With $L_y^* = -0.83$, the whole trailing droplet falls into the spreading film of leading droplet (Figure 13b), which causes y_{uphill}^* and $y_{downhill}^*$ to increase barely. Compared to other occasions, the increasing rate of y_{uphill}^* declines apparently, and $y_{downhil}l^*$ keeps growing up all through the impact process, in other words, a de-wetting process could not be seen. As a result, the contact time reaches a maximum. In Figure 14b, except $L_y^* = -0.83$, a similar evolution of D_y^* at various L_y^* is observed. A sudden increase of D_y^* is presented. Then it reaches a maximum and turns to decrease continuously. At $L_y^* = -2.33$ and 0.67, the D_y^* declined to zero rapidly, causing the shortest contact time. However, for $L_y^* = -0.83$, the D_y^* keeps the peak value for a long time before declining at a steady rate. As a result, the contact time reaches a maximum.

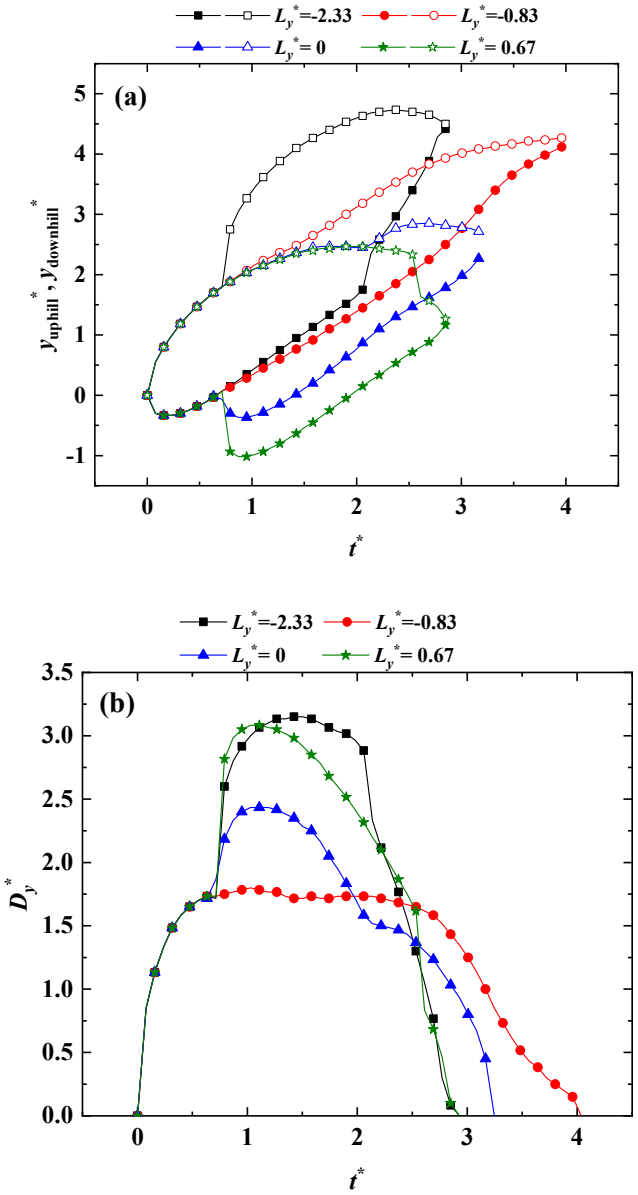

Figure 14. The evolutions of (**a**) y_{uphill}^*; $y_{downhill}^*$; (**b**) D_y^* with time at various L_y^*.

4. Conclusions

In this study, dynamic behaviors of two successive droplets impacting an inclined surface are investigated via a three-dimensional multi-relaxed-time lattice Boltzmann method, aiming to analyze the effects of the velocity ratio of two droplets and the length between the impact points on the contact time on superhydrophobic surface. The effects of various surface wettability and velocity ratios on whether the coalesced droplet rebounds or not are discussed as well. On superhydrophobic surface, when the velocity ratio of two droplets increases, the interaction between the two droplets becomes stronger gradually. When the velocity ratio exceeds a threshold, the contact time increases sharply, because of the coalesced droplet retouching the surface in the retraction process. For a lower contact angle of the surface, it is found that the coalesced droplet cannot rebound and keeps sliding along the surface when the velocity ratio exceeds a critical value. As the contact angle decreases, the critical velocity ratio also decreases. On a superhydrophobic surface, when the length between the impact points of two droplets is longer, a majority of the trailing droplet falls on the surface. The two droplets spread and retract relatively independently, and a fast rebounding is observed. As the length between the impact points decreases, more and more liquid of the trailing droplet lands on the leading droplet. The two droplets merge into a bigger coalesced droplet and rebound finally, leading to a longer contact time. The interaction between droplets is fairly complicated, and more details are deserved to be investigated, such as the squeeze out of gas film during coalescence. Moreover, a quantitative illustration on the energy balance, i.e., kinetic energy, surface energy, and viscous dissipation during spreading and recoiling, is expected in the future.

Author Contributions: Conceptualization, D.-J.L.; Data curation, L.-Z.Z., M.-C.Y., X.W., and S.-R.G.; Formal analysis, D.-J.L.; Funding acquisition, X.-D.W.; Investigation, D.-J.L.; Methodology, D.-J.L., and L.-Z.Z.; Project administration, X.-D.W.; Resources, X.W., S.-R.G. and Y.-R.Y.; Software, M.-C.Y.; Supervision, X.-D.W.; Validation, L.-Z.Z., X.W., and Y.-R.Y.; Visualization, S.-R.G. and Y.-R.Y.; Writing—original draft, D.-J.L.; Writing—review & editing, L.-Z.Z. and M.-C.Y. All authors have read and agreed to the published version of the manuscript.

Funding: This study was partially supported by the State Key Program of National Natural Science of China (No. 51936004), the National Science Fund for Distinguished Young Scholars of China (No. 51525602), the Science Fund for Creative Research Groups of the National Natural Science Foundation of China (No. 51821004), and the Fundamental Research Funds for the Central Universities (No. 2020MS060).

Conflicts of Interest: The authors declare no conflict of interest.

References

1. Rodič, P.; Kapun, B.; Panjan, M.; Milošev, I. Easy and Fast Fabrication of Self-Cleaning and Anti-Icing Perfluoroalkyl Silane Film on Aluminium. *Coatings* **2020**, *10*, 234. [CrossRef]
2. Zhang, Y.; Zhang, J.; Liu, Y. Superhydrophobic Surface with Gamma Irradiation Resistance and Self-Cleaning Effect in Air and Oil. *Coatings* **2020**, *10*, 106. [CrossRef]
3. Yoo, H.; Kim, C. Experimental studies on formation, spreading and drying of inkjet drop of colloidal suspensions. *Colloids Surf. A Physicochem. Eng. Asp.* **2015**, *468*, 234–245. [CrossRef]
4. Zhao, X.; Yin, Z.; Zhang, B.; Yang, Z. Experimental investigation of surface temperature non-uniformity in spray cooling. *Int. J. Heat Mass Transf.* **2020**, *146*, 118819. [CrossRef]
5. Kim, J. Spray cooling heat transfer: The state of the art. *Int. J. Heat Fluid Flow* **2007**, *28*, 753–767. [CrossRef]
6. Khojasteh, D.; Kazerooni, M.; Salarian, S.; Kamali, R.; Kazerooni, N.M. Droplet impact on superhydrophobic surfaces: A review of recent developments. *J. Ind. Eng. Chem.* **2016**, *42*, 1–14. [CrossRef]
7. Antonini, C.; Amirfazli, A.; Marengo, M. Drop impact and wettability: From hydrophilic to superhydrophobic surfaces. *Phys. Fluids* **2012**, *24*, 102104. [CrossRef]
8. Yarin, A. Drop impact dynamics: Splashing, Spreading, Receding, Bouncing. *Annu. Rev. Fluid Mech.* **2006**, *38*, 159–192. [CrossRef]
9. Josserand, C.; Thoroddsen, S.T. Drop Impact on a Solid Surface. *Annu. Rev. Fluid Mech.* **2016**, *48*, 365–391. [CrossRef]
10. Castrejón-Pita, J.R.; Betton, E.S.; Kubiak, K.; Wilson, M.C.T.; Hutchings, I.M. The dynamics of the impact and coalescence of droplets on a solid surface. *Biomicrofluidics* **2011**, *5*, 14112. [CrossRef]

11. Fujimoto, H.; Ogino, T.; Takuda, H.; Hatta, N. Collision of a droplet with a hemispherical static droplet on a solid. *Int. J. Multiph. Flow* **2001**, *27*, 1227–1245. [CrossRef]
12. Fujimoto, H.; Ito, S.; Takezaki, I. Experimental study of successive collision of two water droplets with a solid. *Exp. Fluids* **2002**, *33*, 500–502. [CrossRef]
13. Raman, K.A.; Jaiman, R.K.; Lee, T.-S.; Low, H.-T. Lattice Boltzmann study on the dynamics of successive droplets impact on a solid surface. *Chem. Eng. Sci.* **2016**, *145*, 181–195. [CrossRef]
14. Soltman, D.; Subramanian, V. Inkjet-Printed Line Morphologies and Temperature Control of the Coffee Ring Effect. *Langmuir* **2008**, *24*, 2224–2231. [CrossRef] [PubMed]
15. Stringer, J.; Derby, B. Formation and Stability of Lines Produced by Inkjet Printing. *Langmuir* **2010**, *26*, 10365–10372. [CrossRef] [PubMed]
16. Zhang, L.; Zhu, Y.; Cheng, X. Numerical investigation of multi-droplets deposited lines morphology with a multiple-relaxation-time lattice Boltzmann model. *Chem. Eng. Sci.* **2017**, *171*, 534–544. [CrossRef]
17. Raman, K.A.; Jaiman, R.K.; Lee, T.-S.; Low, H.-T. Dynamics of simultaneously impinging drops on a dry surface: Role of impact velocity and air inertia. *J. Colloid Interface Sci.* **2017**, *486*, 265–276. [CrossRef]
18. Ahmad, S.; Tang, H.; Yao, H. Oblique impact of two successive droplets on a flat surface. *Int. J. Heat Mass Transf.* **2018**, *119*, 433–445. [CrossRef]
19. Graham, P.J.; Farhangi, M.M.; Dolatabadi, A. Dynamics of droplet coalescence in response to increasing hydrophobicity. *Phys. Fluids* **2012**, *24*, 112105. [CrossRef]
20. Damak, M.; Varanasi, K.K. Expansion and retraction dynamics in drop-on-drop impacts on nonwetting surfaces. *Phys. Rev. Fluids* **2018**, *3*, 093602. [CrossRef]
21. Yuan, Z.P.; Wu, X.M.; Hu, Z.F. Rotation of a rebounding-coalescing droplet on a superhydrophobic surface. *Phys. Fluids* **2019**, *31*, 062109. [CrossRef]
22. Chen, H.; Liu, X.; Wang, K.; Liu, H.; Shen, S. Numerical study on dynamic characteristics of double droplets impacting a super-hydrophobic tube with different impact velocities. *Int. J. Comput. Fluid Dyn.* **2019**, *33*, 222–233. [CrossRef]
23. Farhangi, M.M.; Graham, P.J.; Choudhury, N.R.; Dolatabadi, A. Induced Detachment of Coalescing Droplets on Superhydrophobic Surfaces. *Langmuir* **2012**, *28*, 1290–1303. [CrossRef] [PubMed]
24. Mitra, S.; Sathe, M.J.; Doroodchi, E.; Utikar, R.; Shah, M.; Pareek, V.; Joshi, J.B.; Evans, G.M. Droplet impact dynamics on a spherical particle. *Chem. Eng. Sci.* **2013**, *100*, 105–119. [CrossRef]
25. Malgarinos, I.; Nikolopoulos, N.; Gavaises, M. A numerical study on droplet-particle collision dynamics. *Int. J. Heat Fluid Flow* **2016**, *61*, 499–509. [CrossRef]
26. Malgarinos, I.; Nikolopoulos, N.; Gavaises, M. Numerical investigation of heavy fuel droplet-particle collisions in the injection zone of a Fluid Catalytic Cracking reactor, Part I: Numerical model and 2D simulations. *Fuel Process. Technol.* **2017**, *156*, 317–330. [CrossRef]
27. Malgarinos, I.; Nikolopoulos, N.; Gavaises, M. Numerical investigation of heavy fuel droplet-particle collisions in the injection zone of a Fluid Catalytic Cracking reactor, part II: 3D simulations. *Fuel Process. Technol.* **2017**, *156*, 43–53. [CrossRef]
28. Mitra, S.; Evans, G. Dynamic Surface Wetting and Heat Transfer in a Droplet-Particle System of Less Than Unity Size Ratio. *Front. Chem.* **2018**, *6*, 259. [CrossRef]
29. Liu, Y.; Moevius, L.; Xu, X.; Qian, T.; Yeomans, J.M.; Wang, Z. Pancake bouncing on superhydrophobic surfaces. *Nat. Phys.* **2014**, *10*, 515–519. [CrossRef]
30. Regulagadda, K.; Bakshi, S.; Das, S.K. Morphology of drop impact on a superhydrophobic surface with macro-structures. *Phys. Fluids* **2017**, *29*, 82104. [CrossRef]
31. Wang, H.; Liu, C.; Zhan, H.; Liu, Y. Droplet Asymmetric Bouncing on Inclined Superhydrophobic Surfaces. *ACS Omega* **2019**, *4*, 12238–12243. [CrossRef] [PubMed]
32. Aboud, D.G.K.; Kietzig, A.-M. On the Oblique Impact Dynamics of Drops on Superhydrophobic Surfaces. Part I: Sliding Length and Maximum Spreading Diameter. *Langmuir* **2018**, *34*, 9879–9888. [CrossRef] [PubMed]
33. Aboud, D.G.K.; Kietzig, A.-M. On the Oblique Impact Dynamics of Drops on Superhydrophobic Surfaces. Part II: Restitution Coefficient and Contact Time. *Langmuir* **2018**, *34*, 9889–9896. [CrossRef] [PubMed]
34. Qian, Y.H.; D'Humières, D.; Lallemand, P. Lattice BGK Models for Navier-Stokes Equation. *EPL Europhysics Lett.* **1992**, *17*, 479–484. [CrossRef]

35. Zheng, S.; Eimann, F.; Philipp, C.; Fieback, T.; Gross, U. Single droplet condensation in presence of non-condensable gas by a multi-component multi-phase thermal lattice Boltzmann model. *Int. J. Heat Mass Transf.* **2019**, *139*, 254–268. [CrossRef]
36. Zheng, S.; Eimann, F.; Fieback, T.; Xie, G.; Gross, U. Numerical investigation of convective dropwise condensation flow by a hybrid thermal lattice Boltzmann method. *Appl. Therm. Eng.* **2018**, *145*, 590–602. [CrossRef]
37. Guo, Z.; Zheng, C.; Shi, B. Discrete lattice effects on the forcing term in the lattice Boltzmann method. *Phys. Rev. E* **2002**, *65*, 046308. [CrossRef]
38. Li, Q.; Luo, K.H.; Kang, Q.; He, Y.; Chen, Q.; Liu, Q. Lattice Boltzmann methods for multiphase flow and phase-change heat transfer. *Prog. Energy Combust. Sci.* **2016**, *52*, 62–105. [CrossRef]
39. Mohamad, A.A. The Boltzmann Equation. In *Lattice Boltzmann Method*; Springer: London, UK, 2011; Volume 70, pp. 23–24.
40. Zhang, D.; Papadikis, K.; Gu, S. Three-dimensional multi-relaxation time lattice-Boltzmann model for the drop impact on a dry surface at large density ratio. *Int. J. Multiph. Flow* **2014**, *64*, 11–18. [CrossRef]
41. Shi, Y.; Tang, G.; Xia, H. Investigation of coalescence-induced droplet jumping on superhydrophobic surfaces and liquid condensate adhesion on slit and plain fins. *Int. J. Heat Mass Transf.* **2015**, *88*, 445–455. [CrossRef]
42. Lin, D.-J.; Wang, L.; Wang, X.-D.; Yan, W.-M. Reduction in the contact time of impacting droplets by decorating a rectangular ridge on superhydrophobic surfaces. *Int. J. Heat Mass Transf.* **2019**, *132*, 1105–1115. [CrossRef]
43. Li, Q.; Luo, K.H.; Li, X.J. Lattice Boltzmann modeling of multiphase flows at large density ratio with an improved pseudopotential model. *Phys. Rev. E* **2013**, *87*, 053301. [CrossRef] [PubMed]
44. Yuan, P.; Schaefer, L. Equations of state in a lattice Boltzmann model. *Phys. Fluids* **2006**, *18*, 42101. [CrossRef]
45. Rioboo, R.; Marengo, M.; Tropea, C. Time evolution of liquid drop impact onto solid, dry surfaces. *Exp. Fluids* **2002**, *33*, 112–124. [CrossRef]
46. Zhang, D.; Papadikis, K.; Gu, S. Application of a high density ratio lattice-Boltzmann model for the droplet impingement on flat and spherical surfaces. *Int. J. Therm. Sci.* **2014**, *84*, 75–85. [CrossRef]
47. Gu, X.; Gupta, A.; Kumar, R. Lattice Boltzmann Simulation of Surface Impingement at High-Density Ratio. *J. Thermophys. Heat Transf.* **2009**, *23*, 773–785. [CrossRef]
48. Caviezel, D.; Narayanan, C.; Lakehal, D. Adherence and bouncing of liquid droplets impacting on dry surfaces. *Microfluid. Nanofluidics* **2008**, *5*, 469–478. [CrossRef]